Influence of Bulk Microphysics Schemes upon Weather Research and Forecasting (WRF) Version 3.6.1 Nor'easter Simulations

Stephen D. Nicholls[1,2], Steven G. Decker[3], Wei-Kuo Tao[1], Stephen E. Lang[1,4], Jainn J. Shi[1,5], and Karen I. Mohr[1]

[1]NASA-Goddard Space Flight Center, Greenbelt, 20716, United States of America
[2]Joint Center for Earth Systems Technology, University of Maryland, Baltimore, 21250, United States of America
[3]Department of Environmental Sciences, Rutgers University, New Brunswick, 08850, United States of America
[4]Science Systems and Applications, Inc., Lanham, 20706, United States of America
[5]Goddard Earth Sciences Technology and Research, Morgan State University, 21251, United States of America

Correspondence to: Stephen D. Nicholls (stephen.d.nicholls@nasa.gov)

Abstract. This study evaluated the impact of five, single- or double- moment bulk microphysics schemes (BMPSs) on Weather Research and Forecasting model (WRF) simulations of seven, intense winter time cyclones impacting the Mid-Atlantic United States. Five-day long WRF simulations were initialized roughly 24 hours prior to the onset of coastal cyclogenesis off the North Carolina coastline. In all, 35 model simulations (5 BMPSs and seven cases) were run and their associated microphysics-related storm properties (hydrometer mixing ratios, precipitation, and radar reflectivity) were evaluated against model analysis and available gridded radar and ground-based precipitation products. Inter-BMPS comparisons of column-integrated mixing ratios and mixing ratio profiles reveal little variability in non-frozen hydrometeor species due to their shared programming heritage, yet their assumptions concerning snow and graupel intercepts, ice supersaturation, snow and graupel density maps, and terminal velocities lead to considerable variability in both simulated frozen hydrometeor species and radar reflectivity. WRF-simulated precipitation fields exhibit minor spatio-temporal variability amongst BMPSs, yet their spatial extent is largely conserved. Compared to ground-based precipitation data, WRF-simulations demonstrate low-to-moderate (0.217–0.414) threat scores and a rainfall distribution shifted toward higher values. Finally, an analysis of WRF and gridded radar reflectivity data via contoured frequency with altitude (CFAD) diagrams reveals notable variability amongst BMPSs, where better performing schemes favored lower graupel mixing ratios and better underlying aggregation assumptions.

1 Introduction

Bulk microphysical parameterization schemes (BMPSs), within numerical modern weather prediction models (e.g., Weather Research and Forecasting model [WRF; Skamarock et al., 2008]), have become increasingly complex and computationally expensive. Presently, WRF offers BMPS options varying from simplistic, warm rain physics (Kessler, 1969) to multi-phase, six-class, two-moment microphysics (Morrison et al., 2009). Microphysics and cumulus parameterizations drive cloud and precipitation processes within WRF and similar models, which has consequences for radiation, moisture, aerosols, and other simulated meteorological processes. Tao et al. (2011) highlighted the importance of BMPSs in models by summarizing more than 36 published, microphysics-focused studies ranging from idealized simulations to hurricanes to mid-latitude convection. More recently, the observation-based studies of Stark (2012) and Ganetis and Colle (2015) investigated microphysical species variability within United States (U.S.) east coast winter-time cyclones (locally called "nor'easters") and have called for further investigation into how BMPSs impact these cyclones, which motivates this nor'easter study.

A "nor'easter" is a large (~2000 km), mid-latitude cyclone occurring from October to April and is capable of bringing punishing winds, copious precipitation, and potential coastal flooding to the Northeastern U.S. (Kocin and Uccellini 2004; Jacobs

et al., 2005; Ashton et al., 2008). This region is home to over 65 million people and produces 16 billion U.S. dollars of daily economic output (Morath, 2016). Given its high economic output, nor'easter-related damages and disruptions can be extreme. Just ten strong, December nor'easters, between 1980 and 2011, produced 29.3 billion U.S. dollars in associated damages (Smith and Katz, 2013).

Recent nor'easter studies are scarce given the extensive research efforts of the 1980s. These historical studies addressed key environmental drivers including frontogenesis and baroclinicity (Bosart, 1981; Forbes et al., 1987; Stauffer and Warner, 1987), anticyclones (Uccelini and Kocin, 1987), latent heat release (Uccelini et al., 1987), and moisture transport by the low-level jet (Uccellini and Kocin, 1987; Mailhot and Chouinard, 1989). Despite extensive observational analyses, little attention has been given to role of BMPSs in mid-latitude winter cyclones.

Reisner et al. (1998) ran several Mesoscale Model Version 5 winter storm simulations with multiple BMPS options that impacted the Colorado Front Range during the Winter Icing and Storms Project. Double-moment BMPSs produced more accurate simulations of super cooled water and ice mixing ratios than single-moment BMPSs. However, single-moment BMPS based simulations vastly improved when the snow-size distribution intercepts were derived from a diagnostic equation rather than from a fixed value.

Wu and Pretty (2010) investigated how five, six-class BMPSs affected WRF simulations of four polar-low events (two over Japan, two over the Nordic Sea). Their simulations yielded nearly identical storm tracks, but notable cloud top temperature and precipitation errors. Overall, the WRF single-moment BMPS (Hong and Lim, 2006) produced marginally better cloud and precipitation process simulations than those from other BMPSs. For warmer, tropical cyclones, Tao et al. (2011) investigated how four, six-class BMPSs impacted WRF simulations of Hurricane Katrina. They found BMPS choice minimally impacted storm track, yet sea-level pressure varied up to 50 hPa.

Shi et al. (2010) evaluated several WRF single-moment BMPSs during a lake-effect snow event. Simulated radar reflectively and cloud top temperature validation revealed that WRF accurately simulated the onset, termination, cloud cover, and band extent of a lake-effect snow event, however snowfall totals at fixed points were less accurate due to interpolation of the mesoscale grid. Inter-BMPS simulation differences were small because low temperatures and weak vertical velocities prevented graupel generation. Reeves and Dawson (2013) investigated WRF sensitivity to eight BMPSs during a December 2009 lake-effect snow event. Simulated precipitation rates and snowfall coverage were particularly sensitive to BMPSs because vertical velocities exceeded hydrometeor terminal fall speeds in half of their simulations. Vertical velocity differences were attributed to varying BMPS frozen hydrometeor assumptions concerning snow density values, temperature-dependent snow-intercepts, and graupel generation terms.

This study will evaluate WRF nor'easter simulations and their sensitivity to six- and seven-class BMPSs with a focus on microphysical properties and precipitation. The remainder of this paper is divided into three sections. Section 2 explains the methodology and analysis methods. Section 3 shows the results. Finally section 4 describes the conclusions, its implications, and prospects for future research.

2 Methods

2.1 Study design

WRF version 3.6.1 (hereafter W361) solves a set of fully-compressible, non-hydrostatic, Eulerian equations in terrain-following coordinates (Skamarock et al., 2008). Figure 1 shows the four-domain WRF grid configuration for this study with a 45-

, 15-, 5-, and 1.667-km horizontal grid spacing, respectively. Additionally, this configuration includes 61 vertical levels, a 50-hPa (~20 km) model top, two-way domain feedback, and cumulus parametrization is turned off for Domains 3 and 4, which are convection permitting. Notably, the location of Domain 4 adjusts for each case (Fig. 1). Global Forecasting System model operational analysis (GMA) data was used for WRF boundary conditions. The above model configuration (except for the 4th domain) and parameterizations are derived from Nicholls and Decker (2015). Model parameterizations include:

- Longwave radiation: New Goddard Scheme (Chou and Suarez, 1999; Chou and Suarez, 2001)
- Shortwave radiation: New Goddard Scheme (Chou and Suarez, 1999)
- Surface layer: Eta similarity (Monin and Obukhov, 1954; Janjic, 2002)
- Land surface: NOAH (Chen and Dudhia, 2001)
- Boundary layer: Mellor-Yamada-Janjic (Mellor and Yamada 1982; Janjic 2002)
- Cumulus parameterization: Kain-Fritsch (Kain, 2004)

This study investigates the seven nor'easter cases described in Table 1 and shown in Fig. 1. These cases are identical to those in Nicholls and Decker (2015) and represent a small, diverse sample of nor'easter events of varying intensity and seasonal timing. In Table 1, the Northeast Snowfall Impact Scale (NESIS) value serves as proxy for storm severity (1 = notable, 5 = extreme) and is based upon storm duration, population impacted, area affected, and snowfall severity (Kocin and Uccellini, 2004). Early and late season storms (Cases 1, 2, and 7) did not have snow and thus lack a NESIS rating.

Five-day, WRF model simulations for this study were initialized 24 hours prior to the first precipitation impacts in the highly populated Mid-Atlantic region and prior to the onset of rapid, coastal cyclogenesis off of the North Carolina coastline. This starting point provides sufficient time to establish mesoscale circulations, surface baroclinic zones, and sensible and latent heat fluxes (Bosart, 1981; Uccelini and Kocin, 1987; Kuo et al., 1991; Mote et al., 1997; Kocin and Uccellini, 2004; Yao et al., 2008, Kleczek et al., 2014). The first nor'easter-associated precipitation impacts are defined as the first 0.5 mm (~0.02 inch) precipitation reading from the New Jersey Weather and Climate Network (D. A. Robinson, pre-print, 2005) related to the cyclone. A smaller threshold was not used to avoid capturing isolated showers occurring well ahead of the primary precipitation shield.

To investigate BMPS influence upon W361 nor'easter simulations, five BMPS are used (Table 2). These BMPSs include three, six-class, three-ice, single-moment schemes (Lin [Lin6; Lin et al., 1983; Rutledge and Hobbs, 1984], Goddard Cumulus Ensemble [GCE6; Tao et al., 1989; Lang et al., 2007], and WRF single moment [WSM6; Hong and Lim 2006]), a seven-class, four-ice, single-moment Goddard Cumulus Ensemble scheme (GCE7; Lang et al. 2014), and finally, the six-class, three-ice, WRF double-moment scheme (WDM6; Lim and Hong 2010)). In total, 35 model simulations were completed (7 nor'easters x 5 BMPSs).

2.2 Evaluation and analysis techniques

Model evaluation efforts involved comparing WRF model output to GMA, Stage IV precipitation (StIV; Fulton et al. 1998; Y. Lin and K.E. Mitchell, preprints, 2005), and Multi-Radar, Multi-Sensor (MRMS) 3D volume radar reflectivity (Zhang et al. 2016). GMA offers six-hourly, gridded dynamical fields, including water vapor, with global coverage. StIV is a six-hourly, 4-km resolution, gridded, combined radar and rain gauge precipitation product covering the United States. Finally, MRMS is two minute, 1.3-km resolution, gridded 3D volume radar mosaic product derived from S- and C-band radars covering the United States and Southern Canada (Zhang et al. 2016) and it is the operational successor to the National Mosaic and Multi-Sensor QPE (NMQ; Zhang et al. 2011) product. Both StIV and MRMS, however are limited by the detection range of their surface-based assets. All cross comparisons between WRF and these evaluation data were conducted at identical grid resolution.

Analysis of WRF model microphysical, precipitation, and simulated radar output was comprised of three main parts: precipitable mixing ratios and domain-averaged mixing ratio profiles, simulated precipitation, and simulated radar reflectivity.

3

114   Precipitable mixing ratios are calculated for all six microphysical species (vapor, cloud ice, cloud water, snow, rain, and graupel)

115   using the equation for precipitable water:

116    $PMR = \frac{1}{\rho g} \int_{P_{top}}^{P_{sfc}} w \, dp$ (1)

117   In Eq. (1), *PMR* is the precipitable mixing ratio in mm, ρ is the density of water (1,000 kg m^{-3}); *g* is the gravitational constant

118   (9.8 m s^{-2}); p_{sfc} is the surface pressure (Pa), p_{top} is the model top pressure (Pa); *w* is the mixing ratio (kg kg^{-1}); *dp* is the change in

119   atmospheric pressure between model levels (Pa). Only water vapor PMR's are evaluated because all other GMA mixing ratio

120   species are nonexistent and ground and space validation microphysical data are lacking, especially over the data-poor North

121   Atlantic (Li et al., 2008; Lebsock and Su, 2014). Similarly, mixing ratio profiles will only be inter-compared amongst BMPSs

122   because satellite-derived cloud ice profile products (e.g., CloudSat 2C-ICE; Deng et al. 2013) do not directly overpass Domain 4

123   during coastal cyclogenesis for any case. WRF-simulated precipitation fields and their distribution were evaluated against StIV

124   and simulation error was quantified via bias and threat score (critical success index; Wilks, 2011) values. Finally, contoured

125   frequency with altitude diagrams (CFADs) were used to validate WRF-simulated radar reflectivity relative to MRMS similar to

126   the radar validation efforts of Yuter and Houze (1995), Lang et al. (2011) and Lang et al. (2014). A CFAD offers the advantage of

127   preserving frequency distribution information, yet is insensitive to spatio-temporal errors. Additionally, CFAD-based scores were

128   calculated for each height level and with time using Eq (2).

129    $CS = 1 - \frac{\sum |PDF_m - PDF_o|_h}{200}$ (2)

130   In (2), *CS* is the CFAD score and PDF_m and PDF_o (%) are the probability density functions (PDF) at constant height from

131   WRF and MRMS, respectively. The CFAD score ranges between 0 (no PDF overlap) to 1 (identical PDFs).

132   **3. Results**

133   **3.1 Hydrometeor species analysis**

134   Figure 2 displays six classes (water vapor, cloud water, graupel, cloud ice, rain, and snow) of precipitable mixing ratios (mm)

135   from each WRF simulation and GMA and Fig. 3 shows corresponding simulated radar reflectivity (no MRMS on this date) at

136   4,000 m above mean sea level (AMSL) from Case 5, Domain 4 at 06 UTC February 2010. At this time, storm track errors are

137   negligible, the cyclone is centralized within Domain 4, and mixing ratio profiles (Fig. 4) show all hydrometeor species to coincide

138   at 4,000 m AMSL and that snow and graupel mixing ratios approach their maximum values at this height. Figure 5, shows the

139   seven-case composite mixing ratios derived from hourly data during the residence time each nor'easter case in Domain 4 (24-30

140   hours). This composite illustrates that mixing ratio profiles largely preserve their shape, maximum mixing ratio heights, and mixing

141   ratio tendencies (i.e., higher snow mixing ratios in GCE6 and GCE7), but hourly mixing ratio values themselves can vary up to

142   3.5 times higher (QRAIN; WDM6) at a given height than in the seven case composite (Fig. 5). Figures 4 and 5 also contain two

143   black dashed lines denoting the 0°C and -40°C heights, which denote the region where super-cooled water may occur. Although

144   both the super-cooled water fraction and these temperature heights vary hourly, the latter demonstrates little to no inter-BMPS

145   variability. Comparing Figs. 2 and 3 reveals a strong correspondence between radar reflectivity signatures at 4,000 m AMSL and

146   precipitable hydrometeor species, especially rain, graupel, and snow. As seen in Fig. 4, all cloud water and rain above 3,500 m

147   AMSL is super-cooled. Stronger nor'easter-related convection (reflectivity > 35 dBZ) in Fig. 3 best corresponds to precipitable

148   rain and then graupel (Fig. 2) despite the near non-existence of the former at 4,000 m AMSL (Fig. 4). This apparent discrepancy

149   suggests localized enhancement of rain mixing ratios where stronger vertical velocities near convection likely drive the freezing

4

level higher than Fig. 4 indicates. Within the broader precipitation shield (20-35 dBZ), radar reflectivity patterns best correspond to precipitable snow and then precipitable graupel (Fig. 2) for all BMPSs except for Lin6 where this trend is reversed. Although Fig. 4 shows that all five BMPSs loosely agree on amount and height of maximum graupel at 4,000 m AMSL, Lin6 has little to any snow at this level, which likely explains the trend reversal. Inter-BMPS mixing ratio variability both at this level and throughout the troposphere is due to identifiable trends within the underlying assumptions made by BMPSs and will be explained in more detail below.

All evaluated BMPSs share a common heritage with the Lin scheme (Note: Lin6 is a modified form of the original Lin scheme). Amongst the BMPSs, only WDM6 explicitly forecasts cloud condensation nuclei, rain, and cloud water number concentrations, the remaining schemes apply derivative equations for these quantities (Hong et al., 2010). Aside from the above, all five BMPS differ primarily in their treatment of frozen hydrometeors, which is most evident from the nearly identical (exception: WDM6) rain mixing ratio profiles (Figs. 4 and 5) and precipitable water vapor (Fig. 2) and is a result consistent with Wu and Petty (2010). Comparing WSM6 to WDM6 reveals the second moment has little to no effect on precipitable rain coverage area (Fig. 2) yet, precipitable rain is enhanced (Fig.2) and rain mixing ratios drop sharply near the surface.

Similar to rain, precipitable cloud water extent (Fig. 2) and maximum cloud water height (Figs. 4 and 5) barely change, yet mixing ratio amounts (Figs. 2, 4, 5) did vary amongst the BMPSs. These cloud water mixing ratio differences are likely associated with both varying ice supersaturation allowances as described for the Goddard schemes by Chern et al. (2016) and for the WRF schemes by Hong et al. (2010) and assumed cloud water number concentrations (300 cm^{-3} for WSM6). Although WDM6 borrows much of its source code from WSM6, forecasts of cloud condensation nuclei and cloud water number concentrations alter inter-hydrometeor species interactions, which in turn alter cloud water mixing ratios (Hong et al. 2010). The similarly between WSM6 and WDM6 in Figs. 2-4 indicate that forecasted cloud number concentrations for Case 5 are likely close to the 300 cm^{-3} value assumed by WSM6. For the other cases, cloud water mixing ratios did vary between WSM6 and WDM6 indicating that WDM6 cloud water number concentrations did stray from 300 cm^{-3} and therefore cause the apparent differences in composite cloud water mixing ratios (Fig. 5).

Figures 2, 4, and 5 show that precipitable snow and snow mixing ratios vary considerably amongst the BMPSs with Lin6 and GCE6 having the smallest and largest snow amounts, respectively. Dudhia et al. (2008) and Tao et al. (2011) attribute the low snow mixing ratios in Lin6 to its high rates of dry collection of snow by graupel, its low snow size distribution intercept (decreased surface area), and its auto-conversion of snow to either graupel or hail at high mixing ratios. GCE6 turns off dry collection of snow and ice by graupel, greatly increasing the snow mixing ratios at the expense of graupel and reducing snow riming efficiency relative to Lin6 (Lang et al. 2007). Snow growth in GCE6 is further augmented by its assumption of water saturation for the vapor growth of cloud ice to snow (Reeves and Dawson, 2013; Lang et al. 2014). GCE7 addressed the vapor growth issue of GCE6 by introducing snow size and density mapping, snow breakup interactions, a relative humidity (RH)-based correction factor, and a new vertical-velocity-dependent ice super saturation assumption (Lang el al., 2007; Lang et al., 2011; Lang et al., 2014; Chern et al., 2016; Tao et al., 2016). Despite the reduced efficiency of vapor growth of cloud ice to snow due to both the new RH correction factor and the ice super saturation adjustment, the new snow mapping and enhanced cloud ice-to-snow auto-conversion in GCE7 offset this potential reduction, which kept GCE snowfall mixing ratios higher than those in non-GCE BMPSs. Unlike Lin6, WSM6 and WDM6 assume that grid cell graupel and snow fall speeds are identical (Dudhia et al., 2008) and that ice nuclei concentration is a function of temperature (Hong et al., 2008). These two aspects, effectively eliminate the accretion of snow by graupel and increase snow mixing ratios at lower temperatures (Dudhia et al., 2008; Hong et al., 2008). Figures 4 and 5 show the maximum snow mixing ratio height is roughly conserved in all non-Lin6 BMPSs. Lin6's assumption of non-uniform graupel and snow fall

189   speeds and dry collection of snow by graupel reduces snow mixing ratios in the middle troposphere and raises its maximum snow

190   mixing ratio height.

191   Compared to snow, graupel mixing ratios are generally smaller except for Lin6 where unrealistically high dry collection of

192   snow by graupel dominates species growth (Stith et al. 2002). Graupel mixing ratios are lowest in GCE7 due to the net effect of

193   its additions despite the inclusion of a new graupel size map. In particular, the combination of the new snow size map (decrease

194   snow size aloft, increases snow surface area, and enhances vapor growth), the addition of deposition conversion processes

195   (graupel/hail particles experiencing deposition growth at lower temperatures are converted to snow), and a reduction in super

196   cooled droplets available for riming (cloud ice generation is augmented, see below) all favor snow growth at the expense of graupel

197   (Lang et al. 2014; Chern et al., 2016; Tao et al., 2016). Consistent with Reeves and Dawson (2013), WSM6 and WDM6 graupel

198   mixing ratios value are typically 30-50 % of their snow counterparts.

199   Although cloud ice mixing ratios are nearly an order of magnitude smaller than those for snow (GCE6), these mixing ratios

200   still vary greatly amongst the BMPSs as illustrated in Figs. 2, 4, and 5. Cloud ice mixing ratios are highest in GCE7 and lowest in

201   Lin6. Wu and Petty (2010) similarly found low cloud ice mixing ratios in Lin6 simulations and ascribe it to dry collection by cloud

202   ice by graupel and its fixed cloud-ice size distribution. Similar to Lin6, GCE6 uses a monodispersed cloud-ice size distribution (20

203   μm diameter), but assumes vapor growth of cloud ice to snow assuming water saturation conditions (yet supersaturated with

204   respect ice) leading to higher cloud ice amounts and also increased cloud ice to snow conversion rates (Lang et al., 2011; Tao et

205   al., 2016). GCE7 blunts cloud ice-to-snow conversion rates using a RH correction factor which is dependent upon ice

206   supersaturation which is itself dependent up vertical velocity. Additionally, GCE7 also includes contact and immersion freezing

207   terms (Lang et al., 2011), makes the cloud ice collection by snow efficiency a function of snow size (Lang et al., 2011; Lang et al.,

208   2014), sets a maximum limit on cloud-ice particle size (Tao et al., 2016), makes ice nuclei concentrations follows the Cooper curve

209   (Cooper, 1986; Tao et al., 2016), and allows cloud ice to persist in ice subsaturated conditions (i.e., RH for ice $\geq$ 70%) (Lang et al,

210   2011; Lang et al., 2014). Despite the increased cloud ice-to-snow auto conversion rates in GCE7 (Lang et al. 2014; Tao et al.

211   2016), precipitable cloud ice amounts nearly doubled relative to GCE6 (See Fig. 2). Similar to GCE7, WSM6 generates larger

212   cloud ice mixing ratios than Lin6, which Wu and Petty (2010) attribute to excess cloud glaciation at temperatures between 0°C

213   and -20°C and its usage of fixed cloud ice size intercepts. Additionally, both WSM6 and WDM6 include ice sedimentation terms

214   which promote smaller cloud ice amounts (Hong et al., 2008). Despite their varying assumptions, the maximum cloud ice heights

215   for both Case 5 and overall (Figs. 4 and 5) are consistent between BMPSs.

216   **3.2 Stage IV precipitation analysis**

217   Excessive precipitation, whether frozen or not, is one of the most potentially crippling impacts of a nor'easter. Figures 6 and

218   7 show Domain 3, accumulated precipitation, their difference from StIV, and the associated probability and cumulative distribution

219   functions (PDF and CDF, respectively) for Cases 5 and 7 based upon the 24-30 hour residence period of a nor'easter within Domain

220   4. Domain 3 serves are the focus for this section because most of Domain 4 resides close to or outside the StIV data boundaries.

221   Cases 5 and 7 are chosen because of their near-shore tracks (Fig. 1) which affords good StIV data coverage. Table 3 includes threat

222   score and bias information from all seven cases and their associated standard deviation statistics. Both threat score and model bias

223   assume the same 10 mm threshold value, which is approximately the 25th percentile of accumulated precipitation (Figs. 6 and 7).

224   Case 4 threat score and bias values (Table 3) are more than two standard deviations from the composite mean due to its non-

225   coastal storm track (Fig. 1) and thus it is excluded from this analysis. The remaining six cases show WRF to have low-to-moderate

226   forecast skill (Threat score: 0.217 [Lin6] – 0.414 [Lin6]) and to cover too large an area with precipitation values greater than 10

227   mm (bias: 1.47 [Lin6, Case 7] – 4.05 [GCE7, Case 3]) relative to StIV. Inter-BMPS threat score and bias differences are an order

228 or magnitude or less than the values from which they are derived. Consistent with Hong et al. (2010), threat score and bias values
229 from WSM6 are equal to or improved upon by WDM6 due to its inclusion of a cloud condensation nuclei feedback. Overall,
230 WDM6 shows marginally better precipitation forecast skill than other BMPSs (lowest threat score in four out of six cases and
231 lowest mean threat score: 0.322), yet Lin6 is the least biased (lowest bias score in four of out of six cases and lowest mean bias:
232 2.55).

233   PDF and CDF plots from Figs. 6 and 7 show WRF to favor higher precipitation amounts and is consistent with the positive
234 bias scores in Table 3. Previous modelling studies of strong convection by Ridout et al. (2005) and Dravitzki and McGregor (2011)
235 found that both GFS and the Coupled Ocean/Atmosphere Mesoscale Prediction System produced too much light precipitation and
236 too much heavy precipitation, which contrast with the above results. Unlike these two studies, nor'easters track too far offshore to
237 be fully sampled by rain gauge data and S-band weather radars. These two issues could lead to an under bias in StIV data, especially
238 near the data boundaries and suggests that WRF threat scores and biases are likely closer to observations than Table 3 indicates.
239 Marginal changes in accumulated precipitation PDFs and CDFs and threat scores amongst BMPSs are consistent with the
240 investigation of simulated precipitation during warm-season precipitation events and a quasi-stationary front by Fritsch and
241 Carbone (2004) and Wang and Clark (2010), respectively.

242 3.3 MRMS and radar reflectivity analysis

243   Figure 8 shows Domain 3, Case 4 radar reflectivity CFADs constructed during the 24 hour residence time of the nor'easter
244 within Domain 4 (12 UTC 26–27 January 2015). Domain 4 CFADs are not shown here because NOAA radar quality control
245 measures for non-precipitating echoes tend to artificially curtail radar echoes at 5 dBZ, especially near the dataset edges (Jian
246 Zhang, NOAA, personal communication). Domain 4-based CFADs (not shown) depict little to no aggregation and are inconsistent
247 with CFADs from previous convection (Lang et al. 2011, Min et al. 2015) and mid-latitude winter storm (Shi et al. 2010) studies.
248 The larger spatial extent and better radar overlap in Domain 3 leads to more realistic CFADs with aggregation. Case 4 data are
249 shown in Fig. 8 because MRMS data were more readily available and apply the latest MRMS reprocessing algorithm.

250   Figure 8 shows that the MRMS-based CFAD has two distinct frequency maxima: one above and another below 6,000 m
251 AMSL. Model simulations replicate the sub-6,000 m AMSL frequency maxima with varying degrees of success. Below 2,000 m
252 (0°C height), GCE7- and Lin6-based CFADs more closely match the MRMS radar reflectivity probability spectra and correctly
253 show its maximum to occur between 0 and 15 dBZ. Other schemes over broaden this probability spectra and shift its maximum
254 toward higher reflectivity values. Despite this rightward shift, hydrometeor profiles below 2,000 m AMSL (Fig. 4) are similar for
255 all BMPS and that factors including assumed or simulated (WDM6) droplet size distributions or aggregation assumptions may be
256 probable causes.
257   Between 2,000 and 6,000 m all non-GCE7 CFADs incorrectly shift toward higher reflectivity values with increasing height
258 and favor values up to 10 dBZ higher (WSM6) than MRMS. Radar reflectivities at 3,000 m AMSL on 26 January 2015 (Fig. 9)
259 indeed show an overestimation of radar reflectivities in non-GCE7 BMPSs from regions of strong convection off of the North
260 Carolina and New Jersey coastlines near the cold front and warm front, respectively. This rightward bowing of CFADs above the
261 melting layer was also reproduced in Shi et al. (2010) (GCE6) and Min et al. (2015) (WSM6 and WDM6), Similar to these studies,
262 all non-GCE7 schemes seemingly produce too much graupel (Fig. 4) which have stronger reflectivity signatures (See section 3.1).
263 GCE7 has the least graupel as a consequence of its new snow size map, inclusion of deposition processes, reduced super cooled
264 cloud droplets and improved aggregation physics.
265   Above 6,000 m AMSL the WRF-based CFADs all collapse toward smaller reflectivity values. This collapse is well
266 documented in the literature (Shi et al. 2010; Lang et al. 2011, Min et al. 2015) and occurs due to errors stemming from increased

entrainment of ambient air near cloud top and underlying aggregation assumptions made by each BMPS. Although each scheme fully collapses by 7,500 m AMSL, the Goddard-based CFADs indicate a considerably steeper tilt in the maximum frequency core as compared to other schemes, which is a likely byproduct of its higher snowfall mixing ratios (Fig. 4). Once above, 8,000 m AMSL, MRMS radar reflectivity values show a second frequency maxima above 15 dBZ which is not replicated by WRF. Radar reflectivities at 9,000 m AMSL on 26 January 2015 (Fig. 10) show precipitating echoes to occur offshore where the non-precipitating echo filtering applied in MRMS removed weak reflectivities and artificially shifting the CFAD toward higher values.

Finally, CFAD scores (Eq 2) with height and time (Fig. 11) provides a means to evaluate hourly forecast skill at each higher level relative to MRMS. Figure 11 shows Lin6 and GCE7 to have notably improved forecast skill, especially between 2,000 and 4,850 m AMSL where increased graupel mixing ratios and droplet sizes which produced radar reflectivities higher than those from MRMS. Despite their similar CFAD scores, CFAD structures (Fig. 8) and 3,000 m AMSL radar reflectivities (Fig. 9) do suggest that GCE7 produces more realistic results than Lin6 where the rate of dry collection of snow by graupel is unrealistically high. In short, Lin6 produces the right answer for the wrong reason, whereas GCE7 produces the correct answer with a more realistic solution. Between 6,300 and 7,000 and m AMSL, GCE7 CFAD scores fall below all other schemes as a consequence of overly small droplets from its aggregation simulations and cloud entrainment which cut off cloud tops at lower heights. The other six cases produce similar tendencies in their CFAD and CFAD scores as noted above for Case 4, except cloud heights become higher and CFADs become wider with the introduction of stronger convection in early and late season events.

4 Conclusions

The role and impact of five bulk microphysics schemes (BMPSs; Table 2) upon seven, Weather Research and Forecasting model (WRF) winter time cyclone ("nor'easter") simulations (Table 1) are investigated and validated against GFS model analysis (GMA), Stage IV rain gauge and radar estimated precipitation, and the radar-derived, Multi-Radar, Multi-Sensor (MRMS) 3D volume radar reflectivity product. Tested BMPSs include three single-moment, six class BMPSs (Lin6, GCE6, and WSM6), one single-moment, seven class BMPS (GCE7), and one double-moment, six-class BMPS (WDM6). Simulated hydrometer mixing ratios show general similarities for non-frozen hydrometeor species (cloud water and rain) due to their common Lin BMPS heritage. However, frozen hydrometeor species (snow, graupel, cloud ice) demonstrate considerably larger variability amongst BMPSs. This variability results from different assumptions concerning snow and graupel intercepts, degree of allowable ice supersaturation, snow and graupel density maps, and terminal velocities made by each BMPS. WRF-simulated precipitation fields exhibit similar coverage, but tend to favor higher precipitation amounts relative to Stage IV observations resulting in low-to-moderate threat scores (0.217–0.414). Inter-model differences are an order of magnitude or less than the threat score values, but WDM6 does demonstrate marginally better overall forecast skill. Finally, MRMS-based contoured frequency with altitude diagrams (CFADs) and CFAD scores show Lin6 and GCE7 are best in the lower half of the troposphere, where GCE7 most realistically reproduced the maximum frequency core between 5 and 15 dBZ due to its temperature and mixing ratio dependent aggregation and new snow map. However, the overly large growth of graupel by dry collection of snow by graupel does suggest that Lin6 obtains high CFAD scores with a less realistic solution than GCE7. Above 6,300 m AMSL, model simulations approach or exceed their cloud tops where entrainment and hydrometeor sizes differences alter cloud top heights and reflectivity fields and non-precipitating echo filtering in MRMS data make evaluations less meaningful with increasing height above cloud top.

This study has shown that although BMPS choice has minimal impact to the large-scale simulated environment, its effect upon microphysical and precipitation properties of a nor'easter is more profound. No single BMPS demonstrated consistently improved precipitation forecast skill as compared to other schemes, yet differences in their underlying microphysical assumptions does yield

variable forecast skill of simulated radar reflectivity structures amongst the BMPSs when compared to MRMS observations. Follow-on studies could investigate additional nor'easter cases or simulate other weather phenomena (polar lows, monsoon rainfall, drizzle, etc.). Results covering multiple phenomena may provide guidance to model users in their selection of BMPS for a given computational cost. Additionally, potential studies could focus on key aspects of a nor'easter's structure (such as the low-level jet) or validation of model output against current and recently available satellite-based datasets from MODIS (Justice et al., 2008), CloudSat (Stephens et al., 2008), CERES, and GPM (Hou et al. 2014). Finally, other validation methods including object-oriented (Marzban and Sandgathe, 2006) or fuzzy verification (Ebert 2008) could be implemented.

5 Code availability

WRF version 3.6.1 is publically available for download from the WRF Users' Page (http://www2.mmm.ucar.edu/wrf/users/download/get_sources.html).

6 Data availability

GFS model analysis data boundary condition data can be obtained from the NASA's open access, NOMADS data server (ftp://nomads.ncdc.noaa.gov/GFS/Grid3/). Stage IV precipitation data is publically available from the National Data and Software Facility at the University Center for Atmospheric Research (http://data.eol.ucar.edu/cgi-bin/codiac/fgr_form/id=21.093). Daily MRMS data is available from the National Severe Storms Laboratory (http://www.nssl.noaa.gov/projects/mrms/)

7 Author contributions

S. D. Nicholls designed and ran all model simulations and prepared this manuscript. S. G. Decker supervised S. D. Nicholls' research efforts, funded the research, and revised the manuscript. W.-K. Tao, S. E. Lang, and J. J. Shi brought their extensive knowledge and expertise on model microphysics, which helped shape the project methodology and rationalize the results. Finally, K. I. Mohr helped to facilitate connections between the research team, supervised S. Nicholls' research, and was pivotal in revising the manuscript.

8 Acknowledgements

References

Ashton, A. D., Donnely, J. P., and Evans, R. L.: A discussion of the potential impacts of climate change on the shorelines of the Northeastern U.S.A. Mitig. Adapt. Strat. Glob. Change, 13, 719–743, 2008.

Bosart, L. F.: The Presidents' Day Snowstorm of 18–19 February 1979: A subsynoptic-scale event, Mon. Wea. Rev., 109, 1542–1566, 1981.

Chen, F., and Dudhia, J.: Coupling an advanced land-surface/ hydrology model with the Penn State/ NCAR MM5 modeling system. Part I: Model description and implementation, Mon. Wea. Rev., 129, 569–585, 2001.

Chern, J.-D., Tao, W.-K., Lang, S. E., Matsui, T., Li, J.-L. F., Mohr, K. I., Skofronick-Jackson, G. M., and Peters-Lidard, C. D.: Performance of the Goddard multiscale modeling framework with Goddard ice microphysical schemes, J. Adv. Model. Earth Syst., 7, doi:10.1002/2015MS000469, 2016.

Chou, M.-D. and Suarez, M. J.: A solar radiation parameterization for atmospheric research studies. NASA Tech, Memo NASA/TM-1999-104606, 40 pp., 1999.

Chou, M.-D., and Suarez, M. J.: A thermal infrared radiation parameterization for atmospheric studies, NASA Tech. Rep. NASA/TM-1999-10466, vol. 19, 55 pp., 2001.

Deng, M., Mace, G. G., Wang, Z., and Lawson, R. P.: Evaluation of several A-Train ice cloud retrieval products with in situ measurements collected during the SPARTICUS campaign, J. Appl. Meteor. Climatol., 52, 1014–1030, 2013.

Dravitzki, S., and McGregor, J.: Predictability of heavy precipitation in the Waikato River Basin of New Zealand, Mon. Wea. Rev., 139, 2184–2197, 2011.

Dudhia, J., Hong, S.-Y., and Lim, K.-S.: A new method for representing mixed-phase particle fall speeds in bulk microphysics parameterizations, J. Meteor. Soc. Japan, 86A, 33–44, 2008.

Ebert, E. E.: Fuzzy verification of high-resolution gridded forecasts: A review and a proposed framework, Meteor. Applic., 15, 51-64, 2008.

Forbes, G. S., Thomson, D. W., and Anthes, R. A.: Synoptic and mesoscale aspects of an Appalachian ice storm associated with cold-air damming, Mon. Wea. Rev., 115, 564–591, 1987.

Fulton, R. A., Breidenbach, J. P., Seo, D.-J., Miller, D. A., and O'Bannon, T.: The WSR-88D rainfall algorithm. Wea. Forecasting, 13, 377–395. 1998.

Fritsch, J. M., and Carbone, R. E.: Improving quantitative precipitation forecasts in the warm season: A USWRP research and development strategy, Bull. Amer. Meteor. Soc., 85, 955–965, 2004.

Ganetis, S. A. and Colle, B. A.: The thermodynamic and microphysical evolution of an intense snowband during the Northeast U.S. blizzard of 8–9 February 2013. Mon. Wea. Rev., 143, 4104-4125, 2015.

Hong, S -Y., and Lim, J.-O. J.: The WRF single-moment 6-class microphysics scheme (WSM6), J. Korean Meteor. Soc., 42, 129-151, 2006.

Hong, S.-Y., Lim, K.-S. S., Lee, Y.-H., Ha, J.-C., Kim, H.-W., Ham, S.-J., and Dudhia, J.: Evaluation of the WRF double-moment 6-class microphysics scheme for precipitating convection, Adv. Meteor., 2010, doi:10.1155/2010/707253, 2010.

Hou, A. Y., Kakar, R. K., Neeck, S., Azarbarzin, A. A., Kummerow, C. D., Kojima, M., Oki, R., Nakamura, K., and Iguchi, T.: The Global Precipitation Measurement Mission, Bull. Amer. Meteor. Soc., 95, 701–722, 2014.

Jacobs, N. A., Lackmann, G. M., and Raman, S.: The combined effects of Gulf Stream-induced baroclinicity and upper-level vorticity on U.S. East Coast extratropical cyclogenesis, Mon. Wea. Rev., 133, 2494–2501, 2005.

Janjic, Z. I.: Nonsingular implementation of the Mellor–Yamada level 2.5 scheme in the NCEP meso model, NCEP Office Note 437, 61 pp., 2002.

Justice, C. O., Vermote, E., Townshend, J. R. G., Defries, R., et al.: The Moderate Resolution Imaging Spectroradiometer (MODIS): land remote sensing for global change research, IEEE Transactions on Geoscience and Remote Sensing, 36, 1228–1249, 1998.

374 Kain, J. S.: The Kain–Fritsch Convective Parameterization: An Update, J. Appl. Meteor., 43, 170–181, 2004.

375 Kessler, E.: On the distribution and continuity of water substance in atmospheric circulation, Meteor. Monogr., 32, Amer. Meteor.
376   Soc., 84 pp, 1969.

377 Kleczek, M. A., Steenveld, G.-J., and Holtslag, A. A. M.: Evaluation of the Weather Research and Forecasting Mesoscale
378   Model for GABLS3: Impact of boundary-layer schemes, boundary conditions and spin-up, Boundary-Layer Meteorol, 152,
379   213–243, 2014.

380 Kocin, P. J. and Uccellini, L. W.: Northeast snowstorms. Vols. 1 and 2, Meteor. Monogr., No. 54., Amer. Met. Soc., 818 pp., 2004.

381 Kuo, Y. H., Low-Nam, S., and Reed, R. J.: Effects of surface energy fluxes during the early development and rapid intensification
382   stages of seven explosive cyclones in the Western Atlantic. Mon. Wea. Rev., 119, 457–476, 1991.

383 Lang, S., Tao, W.-K., Cifelli, R., Olson, W., Halverson, J., Rutledge, S., and Simpson, J.: Improving simulations of convective
384   system from TRMM LBA: Easterly and westerly regimes, J. Atmos. Sci., 64, 1141–1164, 2007.

385 Lang, S. E., Tao, W.-K., Zeng, X., and Li, Y.: Reducing the biases in simulated radar reflectivities from a bulk microphysics
386   scheme: Tropical convective systems, J. Atmos. Sci., 68, 2306–2320, 2011.

387 Lang, S. E., Tao, W.-K., Chern, J.-D., Wu, D., and Li, X.: Benefits of a fourth ice class in the simulated radar reflectivities of
388   convective systems using a bulk microphysics scheme, J. Atmos. Sci., 71, 3583–3612, doi:10.1175/JAS-D-13-0330.1, 2014.

389 Lebsock, M., and Su, H: Application of active spaceborne remote sensing for understanding biases between passive cloud water
390   path retrievals, J. Geophys. Res. Atmos., 119, 8962–8979, doi:10.1002/2014JD021568, 2014.

391 Li, J.-L. F., Waliser, D., Woods, C., Teixeira, J., Bacmeister, J., Chern, J.-D., Shen, B.-W., Tompkins, A., Tao, W.-K., and
392   Kohler, M.: Comparisons of satellites liquid water estimates to ECMWF and GMAO analyses, 20th century IPCC AR4
393   climate simulations, and GCM simulations, Geophys. Res. Lett., 35, L19710, doi:10.1029/2008GL035427, 2008.

394 Lim, K.-S. and Hong, S.-Y.: Development of an effective double-moment cloud microphysics scheme with prognostic cloud
395   condensation nuclei (CCN) for weather and climate models, Mon. Wea. Rev., 138, 1587–1612, 2010.

396 Lin, Y.-L., Farley, R. D., and Orville, H. D.: Bulk parameterization of the snow field in a cloud model, J. Climate Appl. Meteor.,
397   22, 1065–1092, 1983.

398 Mailhot, J. and Chouinard, C.: Numerical forecasts of explosive winter storms: Sensitivity experiments with a meso-scale model,
399   Mon Wea. Rev., 117, 1311–1343, 1989.

400 Marzban, C., and Sandgathe, S.: Cluster analysis for verification of precipitation fields, Wea. Forecasting, 21, 824–838, 2006.

401 Mellor, G. L., and Yamada, T.: Development of a turbulence closure model for geophysical fluid problems, Rev. Geophys. Space
402   Phys., 20, 851–875, 1982.

403 Min, K.-H., S. Choo, D. Lee, and G. Lee: Evaluation of WRF cloud microphysics schemes using radar observations. Weather and
404   Forecasting, 30, 1571–1589, 2015.

405 Monin, A. S., and Obukhov, A. M.: Basic laws of turbulent mixing in the surface layer of the atmosphere. Tr. Akad. Nauk SSSR
406   Geophiz. Inst., 24, 163–187, 1954.

407 Morath, E.: Will a blizzard freeze U.S. economic growth for the third straight year, Wall Street Journal, 20 Jan. 2016.

408 Morrison, H., Thompson, G., and Tatarskii, V.: Impact of cloud microphysics on the development of trailing stratiform
409   precipitation in a simulated squall line: Comparison of one- and two-moment schemes, Mon. Wea. Rev., 137, 991–1007, 2009.

410 Mote, T. L., Gamble, D. W., Underwood, S. J., and Bentley, M. L.: Synoptic-scale features common to heavy snowstorms in the
411   Southeast United States, Wea. Forecasting, 12, 5–23, 1997.

412 Nicholls, S. D. and Decker, S. G.: Impact of coupling an ocean model to WRF nor'easter simulations, Mon. Wea. Rev., 143, 4997–
413   5016, 2015.

414 Reeves, H. D. and Dawson II, D. T.: The dependence of QPF on the choice of microphysical parameterization for lake-effect
415   snowstorms, J. Appl. Meteor. Climatol., 52, 363–377, 2013.

416 Reisner, J. R., Rasmussen, R. M., and Bruintjes, R .T.: Explicit forecasting of super cooled liquid water in winter storms using the
417   MM5 mesoscale model. Quar. J. Roy. Met. Soc., 124, 1071–1107, 1998.

418 Ridout, J. A., Y. Jin, and Liou, C.-S.: A cloud-base quasi-balance constraint for parameterized convection: Application to the
419   Kain–Fritsch cumulus scheme, Mon. Wea. Rev., 133, 3315–3334, 2005.

420 Rutledge, S. A., and Hobbs, P. V.: The mesoscale and microscale structure and organization of clouds and precipitation in mid-
421   latitude cyclones. XII: A diagnostic modeling study of precipitation development in narrow cloud-frontal rainbands. J. Atmos.
422   Sci., 20, 2949–2972, 1984.

423 Shi, J. J. et al.: WRF simulations of the 20-22 January 2007 snow events of Eastern Canada: Comparison with in situ and satellite
424   observations, J. Appl. Meteor. Climatol., 49, 2246–2266, 2010.

425 Skamarock, W.C., Klemp, J. P., Dudhia, J., Gill, D. O., Barker, D. M., Duda, M. G., Huang, X.-Y., Wang, W., and Powers, J. G.:
426   A description of the advanced research WRF version 3, NCAR Tech. Note NCAR/TN–475+STR, 125 pp., 2008.

427 Smith, A. B., and Katz, R. W.: US billion-dollar weather and climate disasters: Data sources, trends, accuracy and biases,
428   Natural Hazards, 67, 387–410, 2013.

429 Stark, D.: Field observations and modeling of the microphysics within winter storms over Long Island, NY. M.S. thesis, School
430   of Marine and Atmospheric Sciences, Stony Brook University, 132 pp., 2012.

431 Stauffer, D. R., and Warner, T. T.: A numerical study of Appalachian cold-air damming and coastal frontogenesis, Mon. Wea.
432   Rev., 115, 799–821, 1987.

433 Stephens, G. L., et al.: CloudSat mission: Performance and early science after the first year of operation, J. Geophys. Res., 113,
434   D00A18, doi:10.1029/2008JD009982, 2008.

435 Stith, J. L., Dye, J. E., Bansemer, A., Heymsfield, A. J., Grainger, C. A., Petersen, W. A, and Clfelli, R.: Microphysical
436   observations of tropical clouds, J. Appl. Meteor., 41, 97–117, 2002.

437 Tao, W.-K., Simpson, J. and McCumber, M.: An ice-water saturation adjustment, Mon. Wea. Rev., 117, 231–235, 1989.

438 Tao, W.-K., Shi, J. J., Chen, S. S., Lang, S., Lin, P.-L., Hong, S.-Y., Peters-Lidard, C., and Hou, A.: The impact of microphysical
439   schemes on hurricane intensity and track, Asia-Pacific J. Atmos. Sci., 47, 1–16, 2011.

440 Tao, W.-K., Wu, D., Lang, S., Chern, J.-D., Peters-Lidard, C., Fridlind, A., and Matsui, T.: High-resolution NU-WRF simulations
441   of a deep convective-precipitation system during MC3E: Further improvements and comparisons between Goddard
442   microphysics schemes and observations, J. Geophys. Res. Atmos., 121, 1278–1305, doi:10.1002/2015JD023986, 2016.

443 Uccellini, L. W. and Kocin, P. J.: The Interaction of jet streak circulations during heavy snow events along the east coast of the
444   United States, Wea. Forecasting, 2, 289–308, 1987.

445 Wang, S.-Y., and Clark, A. J.: NAM Model forecasts of warm-season quasi-stationary frontal environments in the Central United
446   States, Wea. Forecasting, 25, 1281–1292, 2010.

447 Wilks, D. S.: Statistical methods in the atmospheric sciences, third edition, Academic Press, Oxford, in press., 2011.

448 Wu, L., and Petty, G. W.: Intercomparison of bulk microphysics schemes in model simulations of polar lows, Mon. Wea. Rev.,
449   138, 2211–2228, 2010.

450 Yao, Y., Pierre, W., Zhang, W., and Jiang, J.: Characteristics of atmosphere-ocean interactions along North Atlantic extratropical
451   storm tracks, J. Geophys. Res., 113, doi:10.1029/2007JD008854, 2008.

452 Yuter, S. E., and Houze, R. A.: Three-dimensional kinematic and microphysical evolution of Florida cumulonimbus part II:
453   frequency distributions of vertical velocity, reflectivity, and differential reflectivity, Mon. Wea. Rev., 123, 1941–1963.

Zhang, J., Howard, K., Langston, C., Vasiloff, S., Kaney, B., Arthur, A., et al.: National mosaic and multi-sensor QPE (NMQ) system: description, results, and future plans. Bulletin of the American Meteorological Society, 92, 1321-1338, 2011.

Zhang, J., Howard, K., Langston, C., Kaney, B., Qi, Y., Tang, L., Grams, H., Wang, Y., Cocks, S., Martinaitis, S., and Arthur, A.: Multi-radar multi-sensor (MRMS) quantitative precipitation estimation: Initial operating capabilities. Bull. Amer. Meteor. Soc., 97, 621–638, 2016.

459 **Table 1. Nor'easter case list. The NESIS number is included for storm severity reference. Mean sea-level pressure (MSLP) indicates**
460 **maximum cyclone intensity in GMA. The last two columns denote the first and last times for each model run. GMA storm tracks are**
461 **displayed in Fig. 1.**
462

Case Number	NESIS	MSLP (hPa)	Event Dates	Model Run Start Date	Model Run End Date
1	N/A	991.5	15–16 Oct 2009	10/15 00UTC	10/20 00UTC
2	N/A	989.5	07–09 Nov 2012	11/06 18UTC	11/11 18UTC
3	4.03	972.6	19–20 Dec 2009	12/18 18UTC	12/23 18UTC
4	2.62	980.5	26–28 Jan 2015	01/25 12UTC	01/30 12 UTC
5	4.38	979.7	05–07 Feb 2010	02/05 06UTC	02/10 06UTC
6	1.65	1005.5	02–03 Mar 2009	03/01 00UTC	03/06 00UTC
7	N/A	993.5	12–14 Mar 2010	03/11 18UTC	03/16 18UTC

463
464

465 **Table 2. Applied bulk microphysics schemes and their characteristics. The below table indicates simulated mixing ratio species and**
466 **number of moments. Mixing ratio species include: QV = water vapor, QC = cloud water, QH = hail, QI = cloud ice, QG = graupel, QR**
467 **= rain, QS = snow.**

Microphysics Scheme	QV	QC	QH	QI	QG	QR	QS	Moments	Citation
Lin6	X	X		X	X	X	X	1	Lin et al. (1983); Rutledge and Hobbs (1984)
GCE6	X	X		X	X	X	X	1	Tao et al. (1989); Lang et al. (2007)
GCE7	X	X	X	X	X	X	X	1	Lang et al. (2014)
WSM6	X	X		X	X	X	X	1	Hong and Lim (2006)
WDM6	X	X		X	X	X	X	2 (QC, QR)	Lim and Hong (2010)

468

Threat Score	1	2	3	4	5	6	7	Mean	Mean w/o 4
Lin6	0.289	0.217	0.291	0.091	**0.414**	**0.304**	0.332	0.277	0.308
GCE6	0.286	**0.243**	0.320	0.091	0.406	0.291	0.356	0.285	0.317
GCE7	0.288	0.235	0.319	**0.096**	0.405	0.300	0.337	0.283	0.314
WSM6	**0.293**	0.237	0.315	0.093	0.404	0.292	0.356	0.284	0.316
WDM6	0.290	**0.243**	**0.329**	0.094	0.411	0.299	**0.357**	**0.289**	**0.322**

Bias	1	2	3	4	5	6	7	Mean	Mean w/o 4
Lin6	2.47	**3.53**	**2.72**	7.82	**2.22**	2.9	**1.47**	**3.30**	**2.55**
GCE6	**2.37**	3.88	2.85	8.09	2.26	2.93	1.64	3.43	2.65
GCE7	2.52	4.05	2.85	**7.75**	2.23	2.82	1.57	3.40	2.67
WSM6	2.47	3.75	2.86	8.13	2.26	2.93	1.62	3.43	2.64
WDM6	**2.37**	3.8	2.76	8.09	2.23	**2.82**	1.57	3.37	2.59

T. Score Stats:	All Stdev	0.094	All Mean	0.284			
Threat Score	1	2	3	4	5	6	7
Lin6	0.06	-0.71	0.08	-2.05	1.39	0.22	0.52
GCE6	0.03	-0.43	0.39	-2.05	1.31	0.08	0.77
GCE7	0.05	-0.52	0.38	-2.00	1.29	0.18	0.57
WSM6	0.10	-0.50	0.34	-2.03	1.28	0.09	0.77
WDM6	0.07	-0.43	0.48	-2.02	1.36	0.16	0.78

Bias Stats	All Stdev	2.007	All Mean	3.389			
Bias	1	2	3	4	5	6	7
Lin6	-0.46	0.07	-0.33	2.21	-0.58	-0.24	-0.96
GCE6	-0.51	0.24	-0.27	2.34	-0.56	-0.23	-0.87
GCE7	-0.43	0.33	-0.27	2.17	-0.58	-0.28	-0.91
WSM6	-0.46	0.18	-0.26	2.36	-0.56	-0.23	-0.88
WDM6	-0.51	0.21	-0.31	2.34	-0.58	-0.28	-0.91

473

474

List of Figure Captions

Figure 1. Nested WRF configuration used in simulations. The large panel shows the first 3 model domains (45-, 15-, 5- km grid spacing, respectively). The smaller panels show the location of domain 4 (1.667-km resolution) for each of the seven cases. The colored lines show the cyclone track as indicated by GMA for each nor'easter case.

Figure 2. Domain 4 (1.667 km grid spacing), precipitable mixing ratios (mm) at 06 UTC 06 February 2010. Shown abbreviations for mixing ratios include: QV = water vapor, QC = cloud water, QG = graupel, QI = cloud ice, QR = rain, QS = snow.

Figure 3. Simulated radar reflectivity (dBZ) at 4,000 m above mean sea level and their difference at the same time as Fig. 2.

Figure 4. Domain 4-averaged (1.167-km grid spacing) mixing ratios (kg kg^{-1}), temperature (K), and vertical velocity (cm s^{-1}) at the same time as Fig. 2. . The black dashed lines denote the height above mean sea level (MSL) where the air temperature is 0°C or -40°C. The upper-left panel shows composited and model-averaged profiles of temperature (red line) and vertical velocity (blue). Mixing ratio species abbreviations are QCLOUD (cloud water), QGRAUP (graupel), QICE (cloud ice), QRAIN (rain), QSNOW (snow) and QHAIL (hail).

Figure 5. Domain 4-averaged (1.167-km grid spacing), composite mixing ratios (kg kg^{-1}), temperature (K), and vertical velocities (cm s^{-1}) composited over all seven nor'easter events. The black dashed lines denote the height above mean sea level (MSL) where the air temperature is 0°C or -40°C. The upper-left panel shows composited and model-averaged profiles of temperature (red line) and vertical velocity (blue). Mixing ratio species abbreviations are QCLOUD (cloud water), QGRAUP (graupel), QICE (cloud ice), QRAIN (rain), QSNOW (snow) and QHAIL (hail).

Figure 6. Case 5, 24-hour precipitation accumulation and their differences (mm, small panels) and corresponding probability density and cumulative distribution functions (big panel) of these same data derived from Stage IV and WRF model output. Accumulation period is from 00 UTC 06 February 2010 – 00 UTC 07 February 2010. Shown differences are model - Stage IV (StIV).
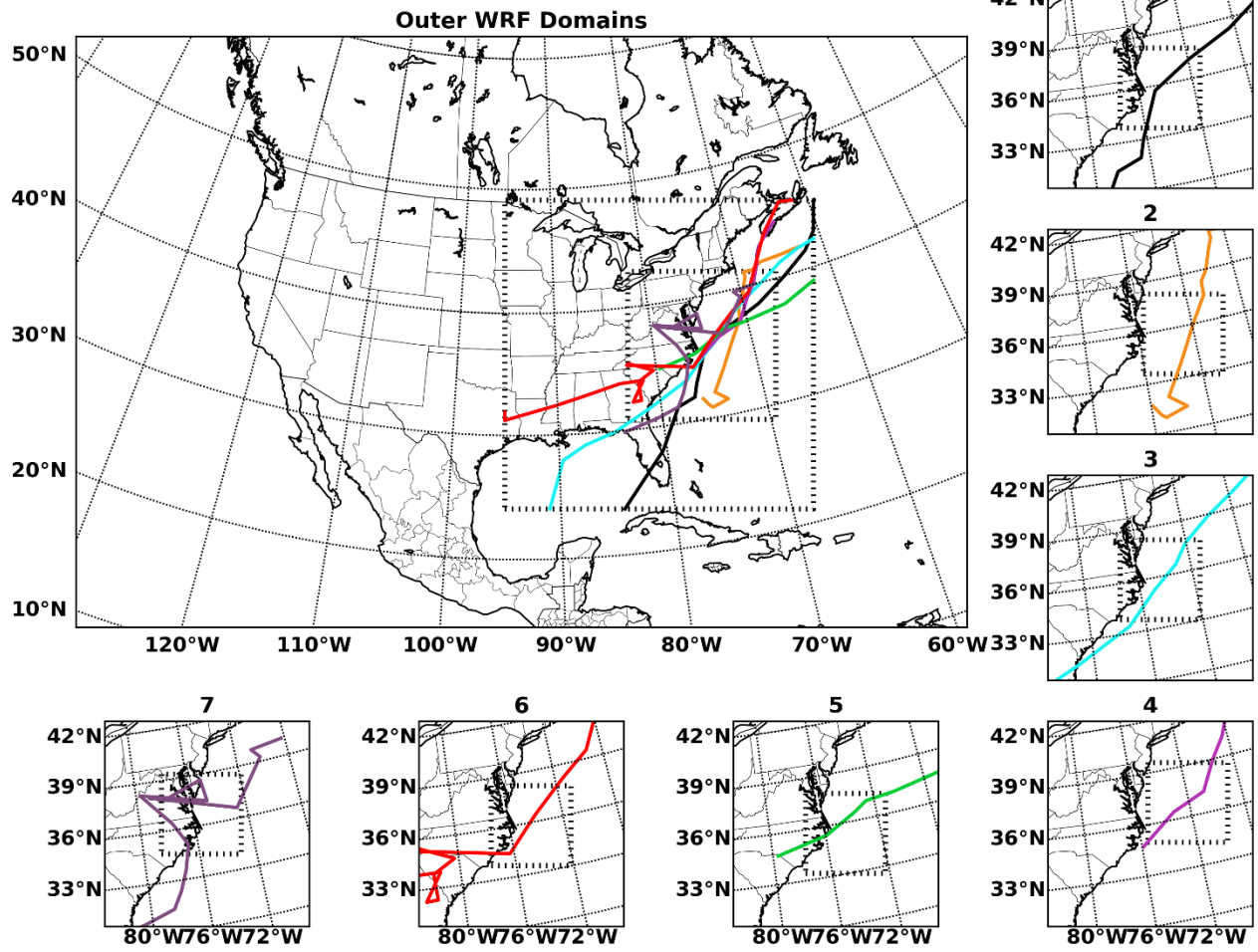
Figure 7. Case 7, 24-hour precipitation accumulation and their differences (mm, small panels) and corresponding probability density and cumulative distribution functions (big panel) of these same data derived from Stage IV and WRF model output. Accumulation period is from 18 UTC 12 March 2010 – 18 UTC 13 March 2010. Shown differences are model - Stage IV (StIV).

Figure 8. Domain 3 (5 km grid spacing), contoured frequency with altitude diagram (CFAD) of radar reflectivity and indicated differences from Case 4 (January 2015). Data accumulation period spans 12 UTC 26 January 2015 – 12 UTC 27 January 2015 during the transit of the nor'easter through Domain 4. The y-axis shows height above mean sea level (HMSL).
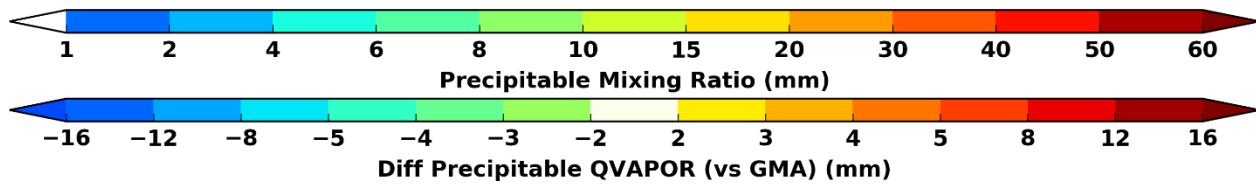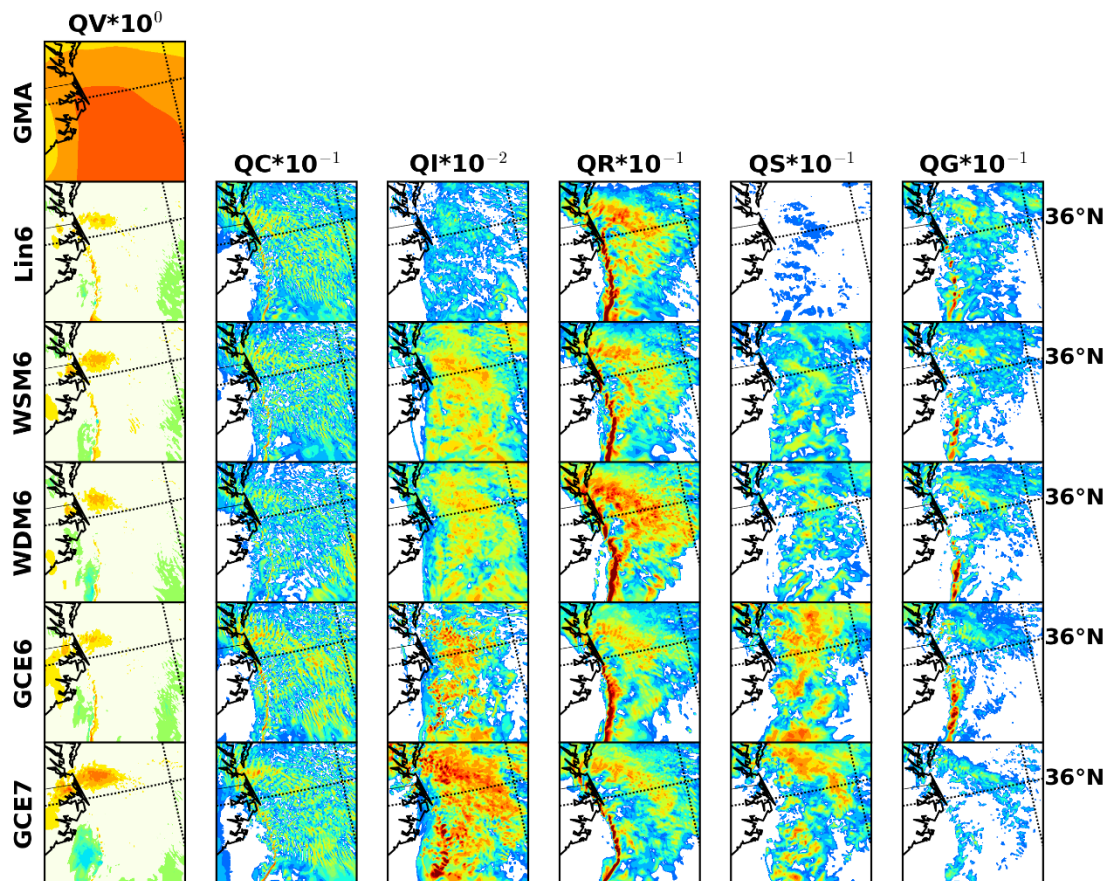
Figure 9. MRMS radar reflectivity and WRF simulated radar reflectivity (dBZ) at 3,000 m above sea level at 18 UTC 26 January 2015. Show radar reflectivity differences are as indicated.

Figure 10. MRMS observed radar and WRF simulated radar reflectivity (dBZ) at 9,000 m above sea level at 18 UTC 26 January 2015. Show radar reflectivity differences are as indicated.
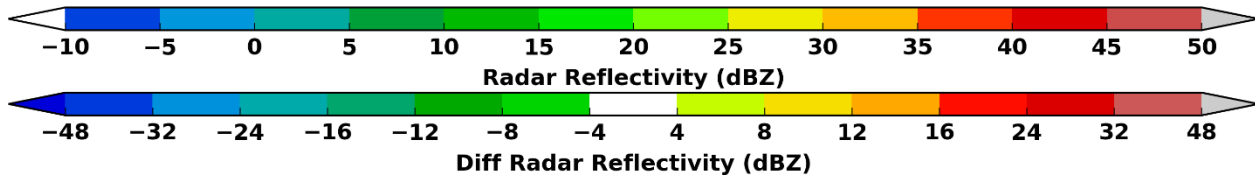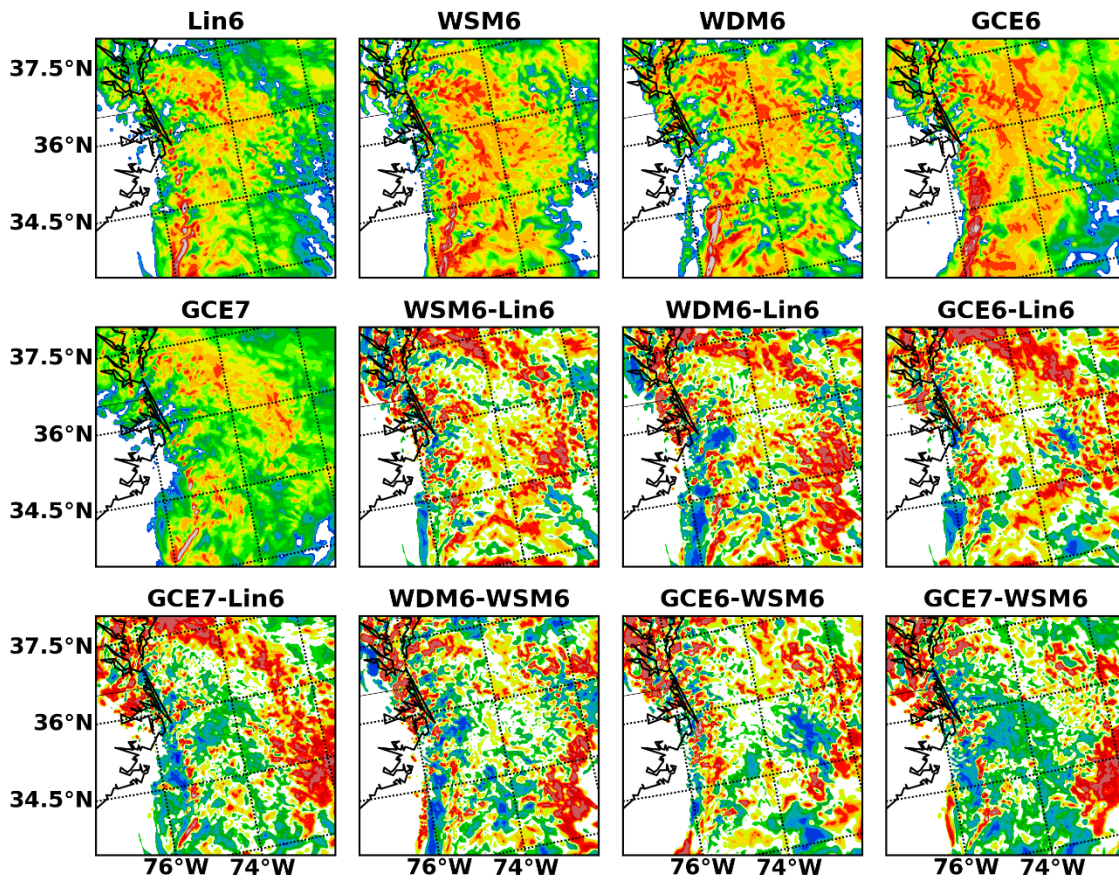
510　　**Figure 11. Domain 3, (5 km grid spacing), hourly CFAD scores (See Eq. 2) of radar reflectivity and indicated differences**

511　　**from Case 4 starting 12 UTC 26 January 2015 and ending on 12 UTC 27 January 2015. The time period corresponds to**

512　　**the same time period as in Figure 5. The y-axis shows height above mean sea level (m).**
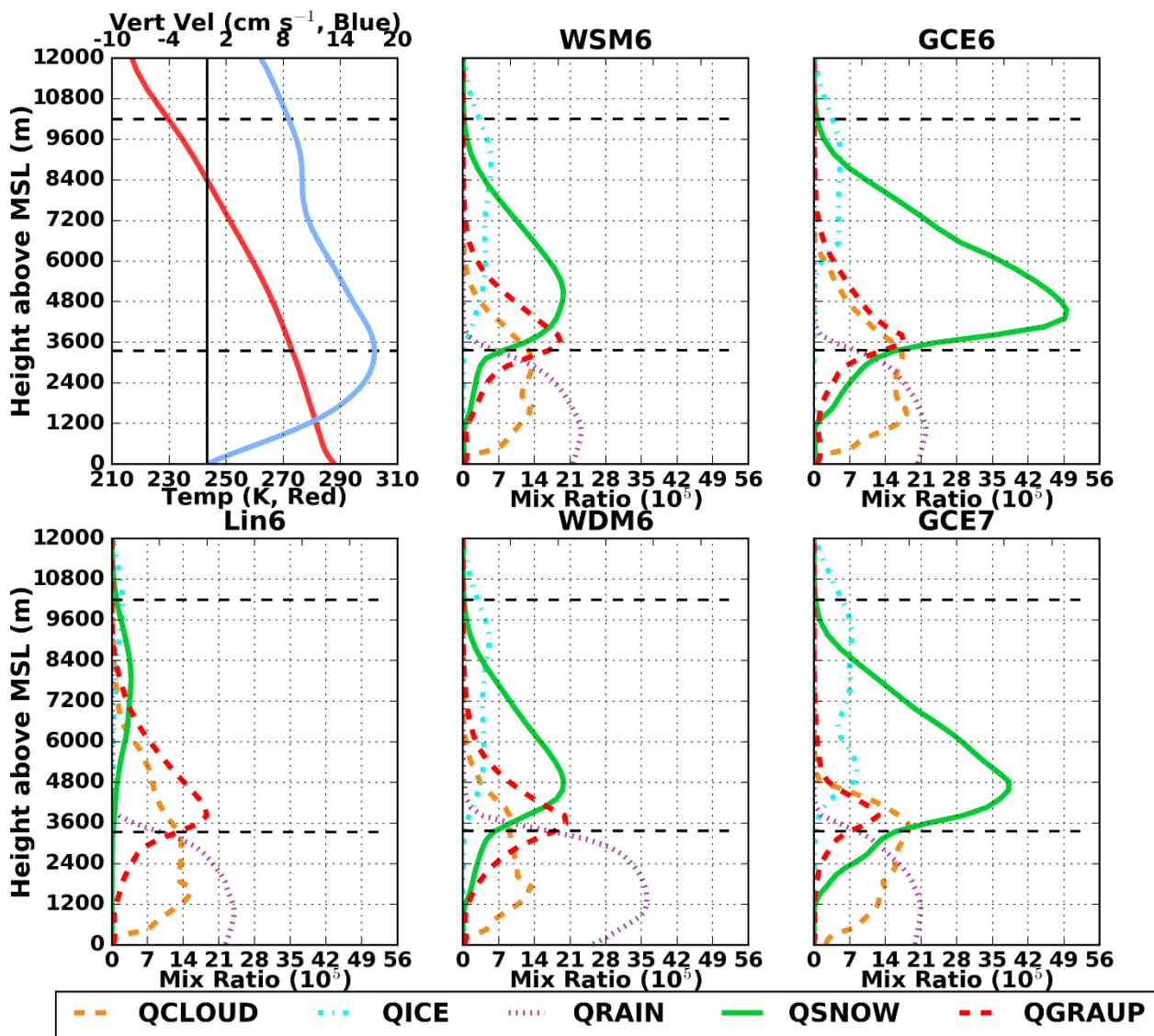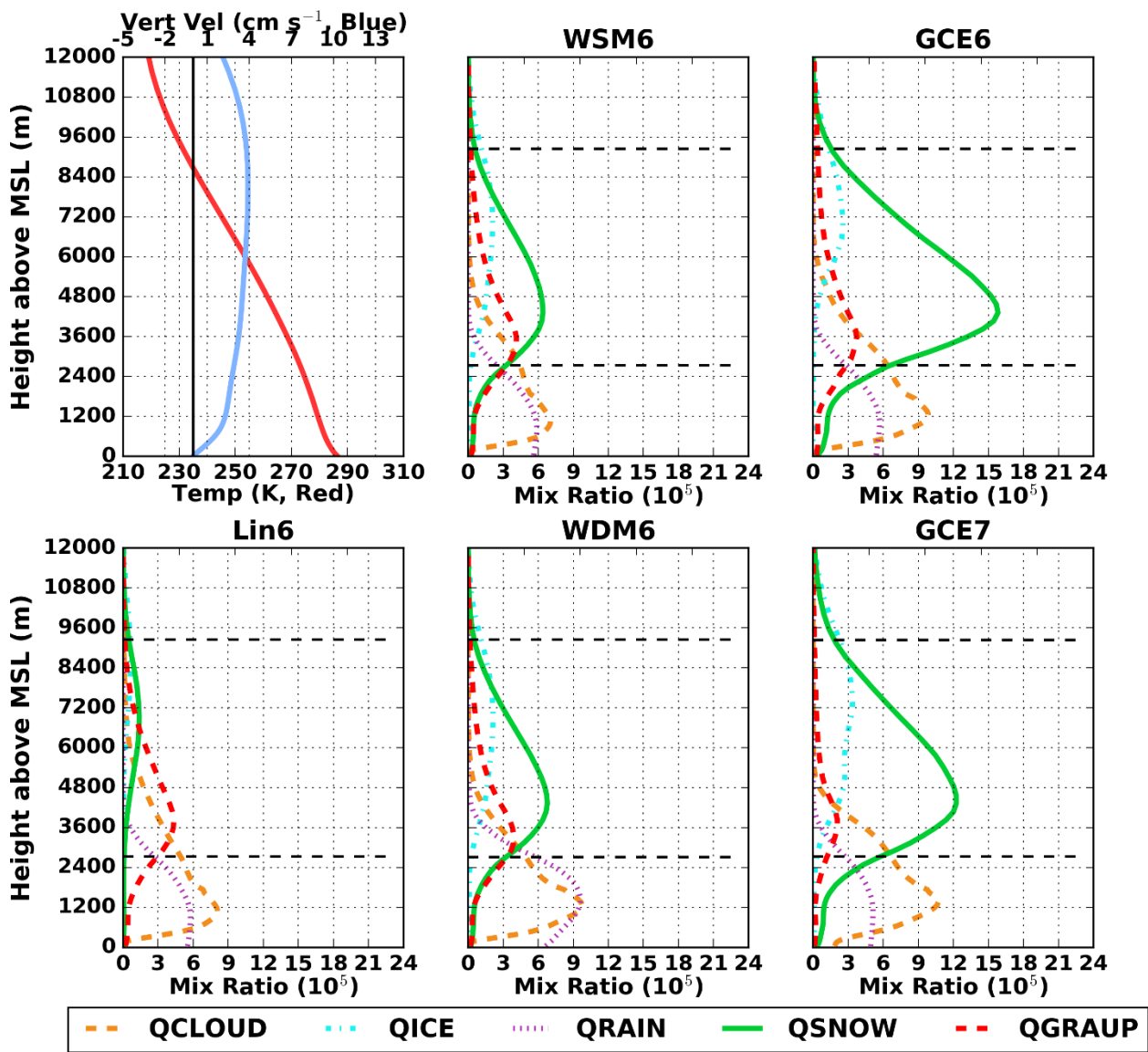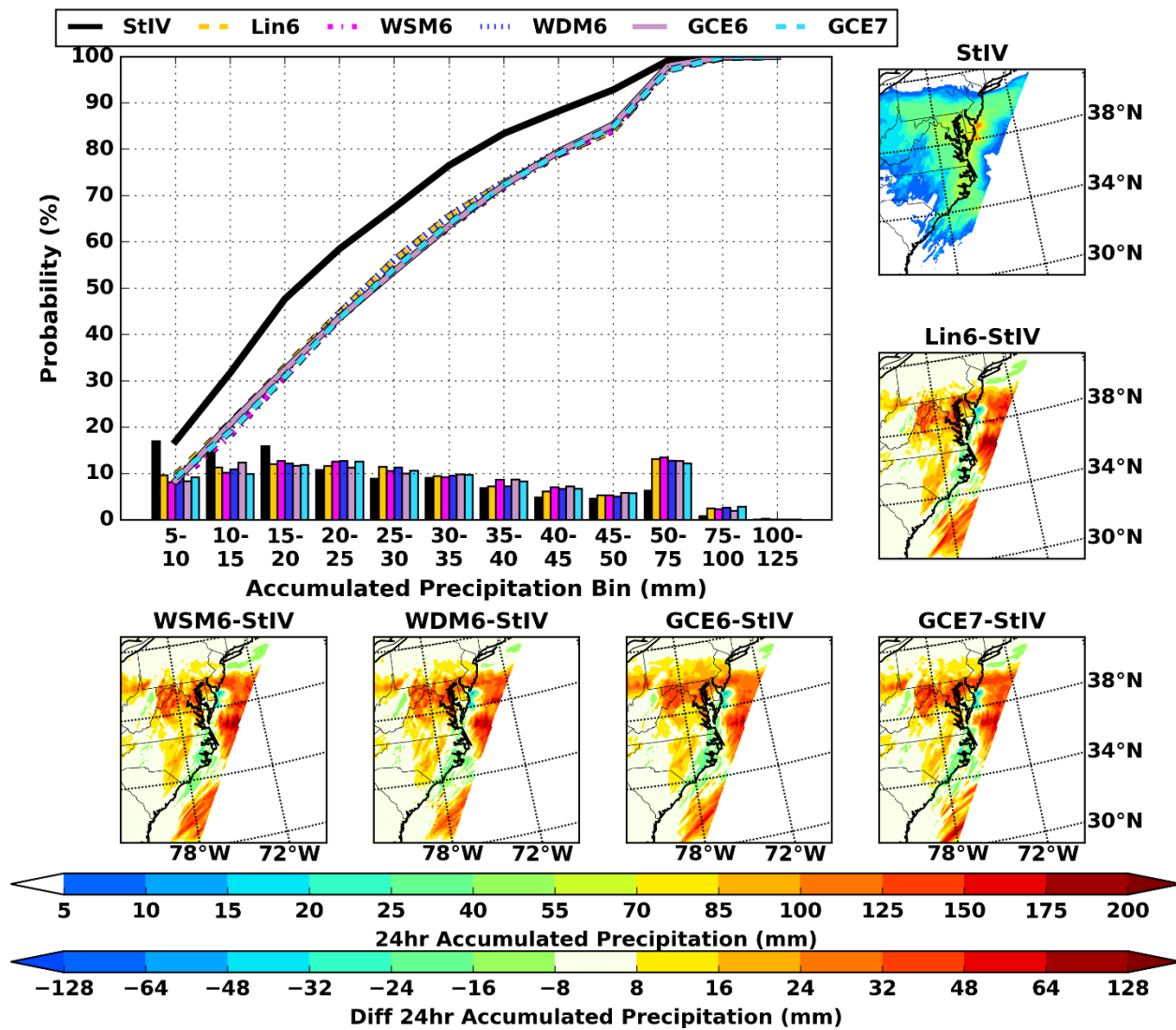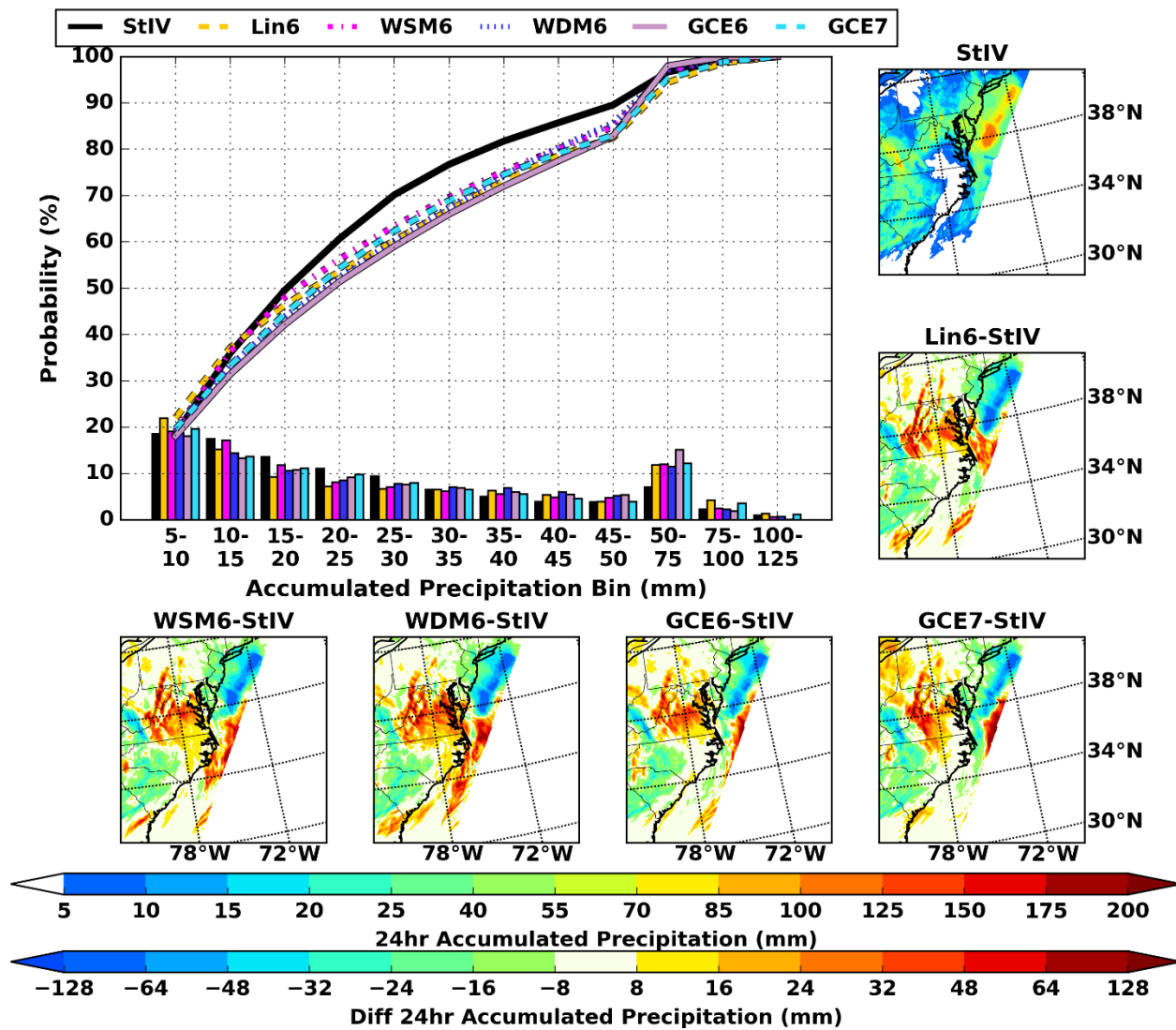
513

514

515

518

521

MRMS Lin6 WSM6 WDM6 GCE6 GCE7 Lin6-MRMS WSM6-MRMS WDM6-MRMS GCE6-MRMS GCE7-MRMS WSM6-Lin6

Radar Reflectivity (dBZ)

−10 −5 0 5 10 15 20 25 30 35 40 45 50

Diff Radar Reflectivity (dBZ)

−48 −32 −24 −16 −12 −8 −4 4 8 12 16 24 32 48

524

Lin6 WSM6 WDM6

GCE6 GCE7 WSM6-Lin6

WDM6-Lin6 GCE6-Lin6 GCE7-Lin6

WDM6-WSM6 WDM6-WSM6 GCE6-WSM6

CFAD Score (vs MRMS)

0.15   0.25   0.35   0.45   0.55   0.65   0.75   0.85   0.95

CFAD Score Difference (vs Lin6)

−0.75 −0.50 −0.40 −0.30 −0.20 −0.10 −0.05 0.05 0.10 0.20 0.30 0.40 0.50 0.75

526